The white matter fiber tract deforms most in the perpendicular direction during *in vivo* volunteer impacts

Zhou Zhou,[1*] Christoffer Olsson,[2] T. Christian Gasser,[3] Xiaogai Li,[1] Svein Kleiven[1]

[1] Division of Neuronic Engineering, KTH Royal Institute of Technology, Stockholm, 14152, Sweden.

[2] Division of Biomedical Imaging, KTH Royal Institute of Technology, Stockholm, 14152, Sweden.

[3] Material and Structural Mechanics, Department of Engineering Mechanics, KTH Royal Institute of Technology, Stockholm, 14152, Sweden.

[*] Corresponding author. Email: zhouz@kth.se

Contact information of other authors:

Christoffer Olsson: chrol@kth.se

T. Christian Gasser: gasser@kth.se

Xiaogai Li: xiaogai@kth.se

Svein Kleiven: sveink@kth.se

Abstract

White matter (WM) tract-related strains are increasingly used to quantify brain mechanical responses, but their dynamics in live human brains during *in vivo* impact conditions remain largely unknown. Existing research primarily looked into the normal strain along the WM fiber tracts (i.e., tract-oriented normal strain), but it is rarely the case that the fiber tract only endures tract-oriented normal strain during impacts. In this study, we aim to extend the *in vivo* measurement of WM fiber deformation by quantifying the normal strain perpendicular to the fiber tract (i.e., tract-perpendicular normal strain) and the shear strain along and perpendicular to the fiber tract (i.e., tract-oriented shear strain and tract-perpendicular shear strain, respectively). To achieve this, we combine the three-dimensional strain tensor from the tagged magnetic resonance imaging (tMRI) with the diffusion tensor imaging (DTI) from an open-access dataset, including 44 volunteer impacts under two head loading modes, i.e., neck rotations (N = 30) and neck extensions (N = 14). The strain tensor is rotated to the coordinate system with one axis aligned with DTI-revealed fiber orientation and then four tract-related strain measures are calculated. The results show that tract-perpendicular normal strain peaks are the largest among the four strain types ($p < 0.05$, Friedman's test). The distribution of tract-related strains is affected by the head loading mode, of which laterally symmetric patterns with respect to the midsagittal plane are noted under neck extensions, but not under neck rotations. Our study presents a comprehensive *in vivo* strain quantification towards a multifaceted understanding of WM dynamics. We find the WM fiber tract deforms most in the perpendicular direction, illuminating new fundamentals of brain mechanics. The reported strain images can be used to evaluate the fidelity of computational head models, especially those intended to predict fiber deformation under non-injurious conditions.

Keywords

Volunteer head impacts, tagged magnetic resonance imaging, diffusion tensor imaging, tract-related strains, *in vivo* white matter fiber deformation

Introduction

Traumatic brain injury (TBI) is a pressing public health and socio-economic problem. Annually, around 69 million people worldwide suffer a TBI.[1] In Europe, about 7.7 million people live with TBI-induced disability, incurring immense personal suffering and huge economic costs.[2] In Sweden, the annual number of TBI-related emergency department visits is estimated to be 30,000 with 10,000 requiring hospitalization.[3] Despite substantial efforts to reduce the occurrence and mitigate the severity, TBI remains to be the leading cause of death in young adults and its incidence is alarmingly increasing in the elderly.[4] There is a clear need for more research to address this TBI-related epidemic, of which how the brain responds during impacts is the central question to be answered.

Various approaches are used to elucidate the biomechanical fundamentals behind brain trauma. In *in situ* cadaveric tests, the post-mortem human subjects are meticulously instrumented to measure brain responses with the impact severity close to the traumatic level.[5] For example, Hardy and colleagues[6,7] conducted 35 cadaveric tests with blunt impacts to track the motion of 12 sparse makers within the deep brain region, which was later analysed to estimate the brain strain[8,9] and strain rate.[10] More recently, Alshareef and coworkers[11] instrumented six head-neck complexes, each of which equipped 24 markers throughout the brain parenchyma, to obtain brain motion in 72 impacts with pure rotational loadings. *In vitro* models play a crucial role in comprehending the mechanobiological cascades of TBI, especially at the cellular and subcellular level, by relating controlled mechanical inputs to the resultant morphological damage or electrical dysfunction of experimental tissues.[12,13] For example, Morrison III and colleagues mechanically injured *in vitro* cultured rat hippocampi. It was found that the cell death was monotonically dependent on the strain,[14] while the functional tolerance was affected by strain and strain rate in a complex fashion.[15] *In silico* head models are increasingly used to quantitatively simulate the localized tissue response during head impacts.[16-18] Modern *in silico* models feature subject-specific geometry,[19,20] anisotropic and heterogeneous brain material,[21-23] and fluid representation of the cerebrospinal fluid.[24-26] Encouraging correlations have been reported between the response of the *in silico* model and experimentally quantified histology or clinically diagnosed injury.[27-30]

Another important line to study human brain biomechanics is *in vivo* quantitative imaging, which can offer complementary information of the intracranial dynamics under non-injurious conditions.[31] Today, many *in vivo* imaging modalities (e.g., magnetic resonance elastography (MRE),[32,33] amplified magnetic resonance imaging (MRI),[34] and phase-contrast MRI)[35] are used to enlighten the brain mechanics under volunteer impacts or physiological conditions, of which the tagged MRI (tMRI) is particularly illuminating. tMRI is an imaging technique that was originally developed to measure cardiovascular deformation.[36] In 2005, Bayly and colleagues[37] pioneeringly implemented tMRI to image brain deformation under sub-injurious occipital impacts. Over the past two decades, tMRI has

been applied to measure brain responses in different voluntary loading scenarios (e.g., axial rotation,[38] frontal impact)[39] with multiple technical advancements to improve imaging efficacy, accuracy, and resolution.[40-43] In 2021, Bayly and colleagues[44] established an open-access dataset, i.e., the Brain Biomechanics Imaging Resource (BBIR) dataset that includes tMRI-recorded brain responses from 50 volunteer tests and other pertinent information (e.g., impact kinematics, structure imaging of volunteers).

Axonal injury is a frequent form of trauma in the white matter (WM) and characterized by diffuse lesions within the fiber tracts usually consisting of oriented axons.[45,46] Given this pathologic feature, there has been growing interest in quantifying the loading endured by the fiber tract.[47] For *in vivo* experimental data, only one study[48] based on the BBIR dataset calculated the normal strain along the fiber tracts (i.e., tract-oriented normal strain, alternatively termed as fiber strain,[49] tract-oriented strain,[50-52] and axonal strain[49,53] in the literature) by projecting the tMRI-recorded brain strain tensor along the primary fiber direction estimated from the diffusion tensor imaging (DTI) in 20 volunteer impacts (10 neck rotations and 10 neck extensions). DTI is an imaging technique in which the anisotropic movement of water molecules within the brain is utilized to estimate the WM fiber tract.[54] Despite interesting results, the tract-oriented normal strain only represents one aspect of fiber deformation. Considering the tensorial nature of the strain and the complexity of impact loading, it is rarely the case that the fiber only endures the tract-oriented normal strain. A multifaceted quantification of fiber deformation remains to be performed.

The current study aims to present a comprehensive quantification of WM tract-related deformation under volunteer impacts. To this end, the tMRI-recorded brain strain tensor data in 44 volunteer tests is related to the DTI-derived fiber direction. These volunteer tests and relevant data are acquired from the open-accessed BBIR dataset.[44,48] By combining multimodal imaging analyses with continuum mechanics, we quantify the normal strain and shear strain along and perpendicular to the fiber tract. This investigation finds the WM tract deforms most in the perpendicular direction, unravelling new fundamentals of brain mechanics. The reported strain data can be used to evaluate the biofidelity of *in silico* models.

Methods

Volunteer tests and imaging data

The brain strain tensor data during volunteer tests and brain imaging are acquired from the publicly available BBIR dataset where details regarding study approval, subject recruitment, test protocol, imaging acquisition, and processing are available elsewhere.[44] Briefly, the volunteer was rapidly rotated at non-injurious levels by a custom-built neck rotation device (rotation within the axial plane along the inferior-superior axis) or neck extension device (rotation within the sagittal plane about the left-right axis). The angular kinematics within the primary rotating plane were recorded, i.e., the axial

plane for the neck rotation (Fig 1A) and the sagittal plane for the neck extension (Fig 1B). In each test, three-dimensional (3D), full-field, time-varying brain strain tensor, including six independent components (Fig 1C), were measured using tMRI at a spatial resolution of 1.5 mm or 2.0 mm and a temporal resolution of 18 ms, 19.5 ms or 20 ms. These subject-specific tensorial brain strain data under known head loading conditions were further complemented by multimodal structural imaging data of the same subject. As the WM is the structure of interest in the current study, DTI and brain segmentation are particularly relevant. In the dataset, DTI-derived information, including the principal eigenvector of the diffusion tensor and the fractional anisotropy (FA) map (Fig 1D), were available. The brain was segmented into different anatomical structures (Fig 1E), of which the WM region included cerebral WM, cerebellar WM, and brainstem. For each test, the structural images were processed with the same spatial resolutions as the tMRI.

In the current study, 44 volunteer tests are included to estimate the WM tract-related strains. Note that, from the 50 tests in the original dataset, 4 tests performed on cadavers and 2 tests without DTI are excluded. These 44 tests, including 30 neck rotations and 14 neck extensions, were acquired from 38 subjects (20 male, 18 female) with an average age of 31.7 ± 10.8 years (range: 19-59 years). Structural imaging data (e.g., brain segmentation, DTI, and its derivatives) are spatially aligned with the tMRI-derived brain strain tensor data, except for 4 tests with imaging misalignment. Co-registrations between different imaging modalities are performed on these 4 tests, with the use of common neuroimaging tools from the FMRIB Software Library.[55,56]

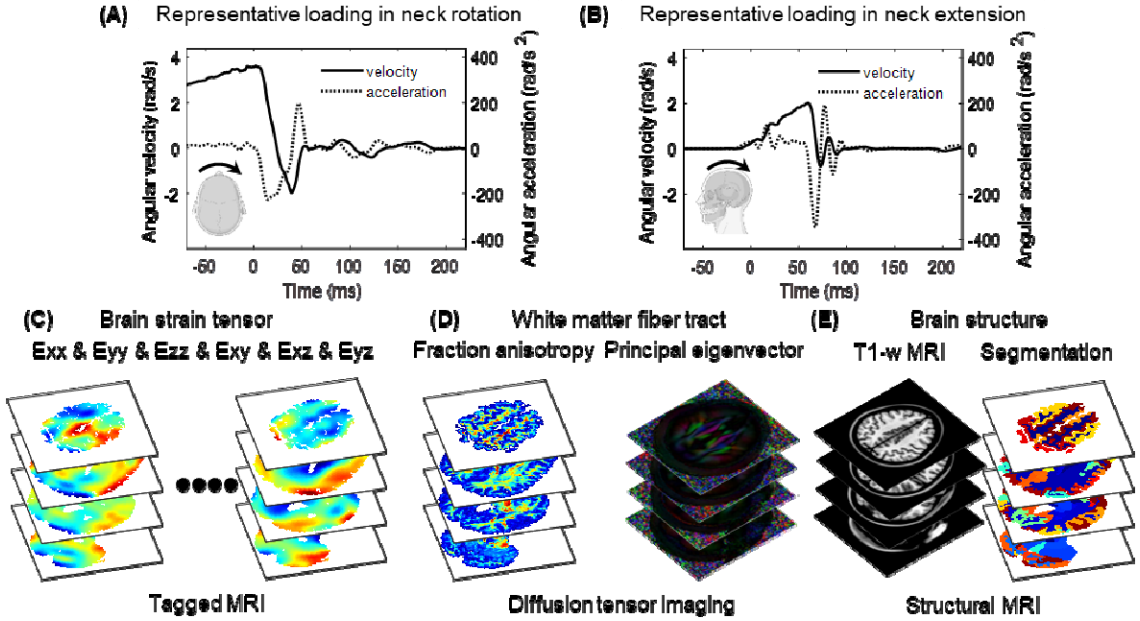

Fig 1. Data from voluntary tests in neck rotation and neck extension and imaging acquisition obtained from the Brain Biomechanics Imaging Resource dataset (https://www.nitrc.org/projects/bbir/).[44,48] (A) Angular kinematics in the axial plane for one representative neck rotation test. (B) Angular kinematics in the sagittal plane for one representative neck extension test. (C) 3D full-field, time-varying Green-Lagrange brain strain tensor measured by tagged MRI. (D) White matter fiber-related information (i.e., fractional anisotropy, and principal eigenvector quantifying the primary direction of fiber tracts) derived from diffusion tensor imaging. (E) Brain structure and

segmentation. Note that the kinematics in subfigures A and B correspond to the two impacts that are used as representative tests for illustration purposes in the "Results" section.

Computation of white matter tract-related strains

To calculate the WM tract-related deformation, the tMRI-derived brain strain tensor is rotated to the coordinate system with one axis aligned with the DTI-derived fiber orientation (referred to as tract-aligned coordinate system), through which the components in the transformed tensor quantify multiple strain modes endured by the fiber (Fig 2). This calculation is applied to all WM voxels (i.e., voxels with FA values ≥ 0.2), of which the fiber orientation is approximated as the first principal eigenvector of the diffusion tensor. In each time frame of tMRI, we calculate the tract-oriented normal strain ( ), a metric that has also been chosen as the parameter of interest in one early *in vivo* study.[48] As a step further, we also study three new tract-related strains, including tract-perpendicular normal strain (, the maximal normal strain perpendicular to the fiber tract), tract-oriented shear strain (, the shear strain along the fiber tract), and tract-perpendicular shear strain (, the maximal shear strain perpendicular to the fiber tract). As magnitudes of strain components are dependent on the choice of tract-aligned coordinate systems, two notations, and , are introduced, representing their maximum values. This calculation is performed at each time frame of the tMRI. The mathematical derivation of tract-related strains is detailed in Appendix A.

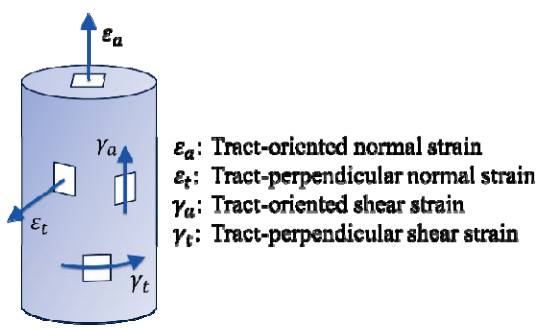

Fig 2. Sketch of four tract-related strains characterizing the normal strain and shear strain along and perpendicular to the fiber tract.

For the four tract-related strains, we identify the peak values accumulated over time during the two head loading protocols (i.e., neck rotation and neck extension). This is motivated since the time-accumulated strain peaks are often used for injury analysis.[57,58] It is also a compromised strategy to address the disparity of temporal resolution in tMRI (30 tests with a time resolution of 18 ms vs. 3 tests with a time resolution of 19.5 ms vs. 11 tests with a time resolution of 20 ms). For the spatial resolution disparity of tMRI (31 tests with a voxel resolution of 1.5 mm vs. 13 tests with a voxel resolution of 2 mm), its influence on the tract-related strains remains negligible, see Appendix B. Hence, strain results with different temporal and spatial resolutions are combined for the statistical analysis. For each test, the peak tract-related strains are computed for three WM subregions (i.e., cerebral WM, cerebellar WM, brainstem) and the whole WM. To avoid potential artifacts, the 95th percentile peak values are reported, the same strategy as in previous studies.[48,59]

Statistical analysis

Whether magnitudes of four tract-related strains (non-normally distributed) differ are tested using the Friedman's test with the Bonferroni correction for multiple comparisons to determine if differences between individual strain pairs are statistically significant. This test is performed at the regional level (i.e., cerebral WM, cerebellar WM, brainstem) and the whole WM level. To compare the fiber deformation between two head loading modes (i.e., neck rotation and neck extension), Mann-Whitney U tests are conducted on four tract-related strain peaks. Within each head loading mode, we perform Pearson's correlations to test the dependency of four tract-related strains at 4 regions of interest (i.e., cerebral WM, cerebellar WM, brainstem, and whole WM) on two angular kinematic peaks (i.e., peak change in angular velocity and peak angular acceleration). 32 Pearson's correlations are conducted for a given head loading mode with the Benjamini-Hochberg method implemented to consider the correction for multiple comparisons.

Results

At the individual level, tract-related strain responses in one specific subject, who performed both a neck rotation and a neck extension, are reported in Fig 3 as illustrative cases. The peak change in angular velocity and peak angular acceleration are 5.6 rad/s and 226.8 rad/s^2 for the neck rotation (Fig 1A), and 2.8 rad/s and 345.6 rad/s^2 for the neck extension (Fig 1B). Spatially heterogeneous strain patterns are noted in the WM and the regions with high strains (i.e., areas in red in Fig 3A and Fig 3C) are dependent on the head loading mode and strain type. For neck rotation, high tract-oriented normal and shear strains are sparsely distributed and mostly occur at the boundary of cerebral WM and periventricular region, while high tract-perpendicular normal and shear strains exhibit relatively continuous patterns that extend from the anterior-superior site in the left cerebrum to the deep region in the right cerebrum (Fig 3A). In the neck extension, high tract-oriented normal strain is primarily noted in the brainstem, while high tract-perpendicular normal and shear strains, tract-oriented shear strain appear isolated and occur mostly in the anterior-superior cerebral region (primarily close to the midsagittal plane), inferior cerebellar area, and brainstem (Fig 3C). For the strain peak in the neck rotation (Fig 3B) and neck extension (Fig 3D), the largest value is consistently noted in tract-perpendicular normal strain across all examined regions (i.e., cerebral WM, cerebellar WM, brainstem, and whole WM).

Left-right symmetric strain patterns with respect to the midsagittal plane are noted in the neck extension (Fig 3C), but not in the neck rotation (Fig 3A). This is further quantified by calculating the strain peaks in the left and right brain hemispheres, respectively (Fig 4). In the neck rotation, the strain differences (in absolute percentage) between the left and right brain hemispheres ranges from 2.7% to 34.8%, while in the neck extension, the percentage of inter-hemispheric strain differences varies from 0.3% to 15.4%.

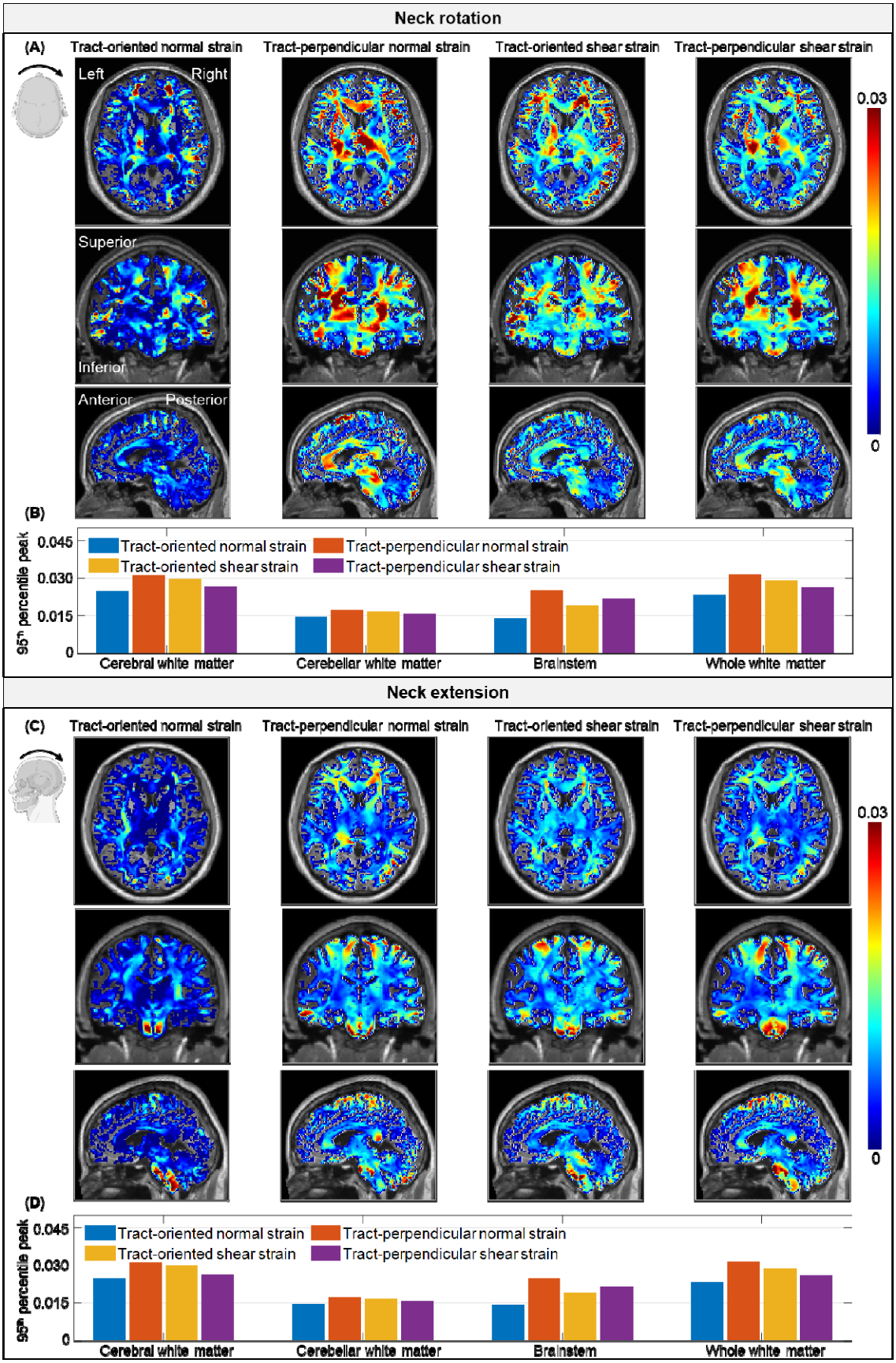
Neck rotation
(A)
Tract-oriented normal strain
Tract-perpendicular normal strain
Tract-oriented shear strain
Tract-perpendicular shear strain
Left
Right
Superior
Inferior
Anterior
Posterior
0.03
0
(B)
95th percentile peak
0.045
0.030
0.015
0
Tract-oriented normal strain
Tract-perpendicular normal strain
Tract-oriented shear strain
Tract-perpendicular shear strain
Cerebral white matter
Cerebellar white matter
Brainstem
Whole white matter
Neck extension
(C)
Tract-oriented normal strain
Tract-perpendicular normal strain
Tract-oriented shear strain
Tract-perpendicular shear strain
0.03
0
(D)
95th percentile peak
0.045
0.030
0.015
0
Tract-oriented normal strain
Tract-perpendicular normal strain
Tract-oriented shear strain
Tract-perpendicular shear strain
Cerebral white matter
Cerebellar white matter
Brainstem
Whole white matter

200

Fig 3. Time-accumulated tract-related strain peaks in one neck rotation (A-B) and one neck extension (C-D) that were conducted on the same subject. (A) Axial, coronal, and sagittal views of tract-oriented normal strain, tract-perpendicular normal strain, tract-oriented shear strain, tract-perpendicular shear strain (color), and T1-w MRI (grayscale) during neck rotation with 95th percentile peak values in three white matter subregions and the whole white matter shown in subfigure B. Similar plots are presented for neck extension in subfigures C-D. The anatomical orientation is specified in the tract-oriented normal strain contour during neck rotation in subfigure A.

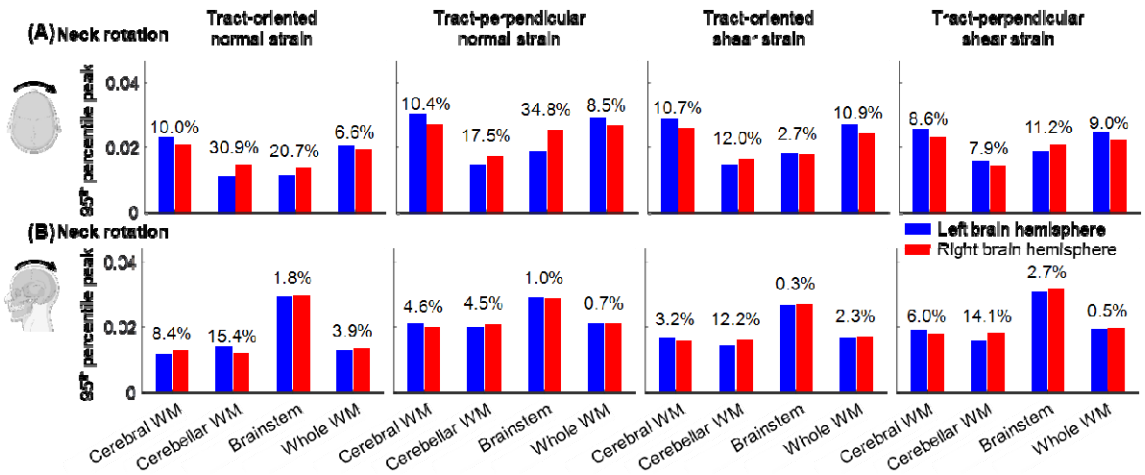

Fig 4. Comparisons of time-accumulated tract-related strain peaks between the left and right brain hemispheres in one neck rotation (A) and one neck extension (B) at three white matter (WM) subregions (i.e., cerebral WM, cerebellar WM, brainstem) and the whole WM level. For each comparison, the strain difference in absolute percentage is labelled with the result from the right brain as the baseline.

At the group level, comparisons among four tract-related strain peaks are summarized in Fig 5. Across all regions of interest, significant differences are noted in magnitudes of tract-related strains (p<0.05, Friedman's tests with the Bonferroni correction of multiple comparisons) with the tract-perpendicular normal strain peak being the largest. The tract-oriented normal strain is significantly smaller than the tract-oriented shear strain and tract-perpendicular shear strain in the cerebral WM, cerebellum WM, and whole WM level, but not in the brainstem. No significant differences are noted between the tract-oriented shear strain and tract-perpendicular shear strain in all examined regions. Detailed plots of inter-strain comparison are presented in Appendix C.

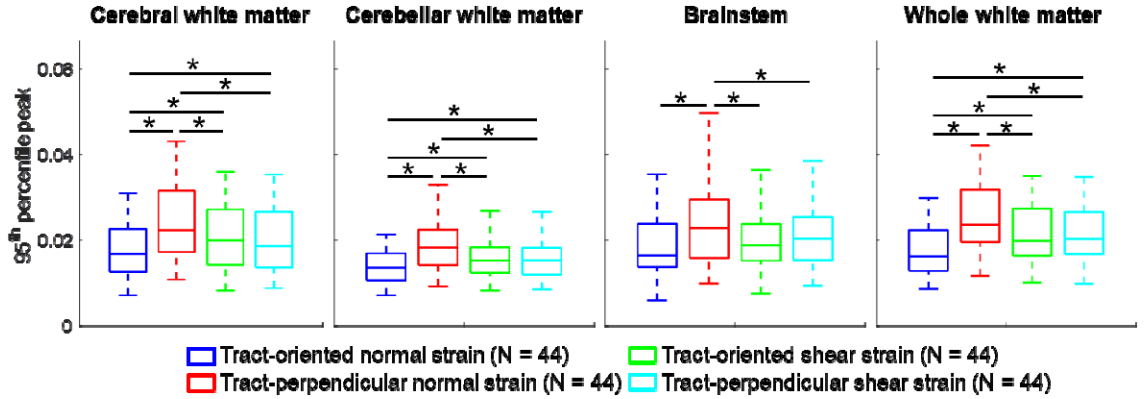

Fig 5. Comparisons of four tract-related strain peaks (95th percentile values) in cerebral white matter (WM), cerebellar WM, brainstem, and the whole WM (* indicates the difference in the referred strain pair is statistically significant when assessed by the Friedman's tests with the Bonferroni correction of multiple comparisons).

Comparisons of tract-related strain peaks between neck rotations and neck extensions is analyzed in Fig 6. The average values for the peak change in angular velocity and peaking angular acceleration are 4.2 ± 1.2 rad/s (range: 1.8-6.4 rad/s) and 185.5 ± 59.2 rad/s^2 (range: 49.8-317.0 rad/s^2) for neck rotations, and 2.1 ± 0.5 rad/s (range: 1.0~2.8 rad/s) and 228.6 ± 8.3 rad/s^2 (range: 63.8-345.6 rad/s^2) for neck extensions. A significant difference (p<0.001) is noted for the peak change in angular velocity between two head loading modes (Fig 6A). A summary of tract-related strains in different WM areas is reported in Fig 6B. At the whole WM level, 95th percentile maximum tract-related strains (mean ± standard deviation (range)) in neck rotations are 0.020 ± 0.005 (0.009-0.030) for tract-oriented normal strain, 0.028 ± 0.007 (0.011-0.042) for tract-perpendicular normal strain, 0.024 ± 0.006 (0.010-0.035) for tract-oriented shear strain, and 0.023 ± 0.006 (0.010~0.035) for tract-perpendicular shear strain. For neck extensions, the maximum tract-oriented normal, tract-perpendicular normal, tract-oriented shear, and tract-perpendicular shear strains are 0.013 ± 0.002 (0.009-0.017), 0.019 ± 0.004 (0.012-0.024), 0.016 ± 0.003 (0.010-0.020), and 0.017 ± 0.003 (0.011-0.022), respectively. When comparing the strain peaks between neck rotations and neck extensions, significant differences (p<0.001) are noted in the cerebral WM and whole WM, independent of the strain type.

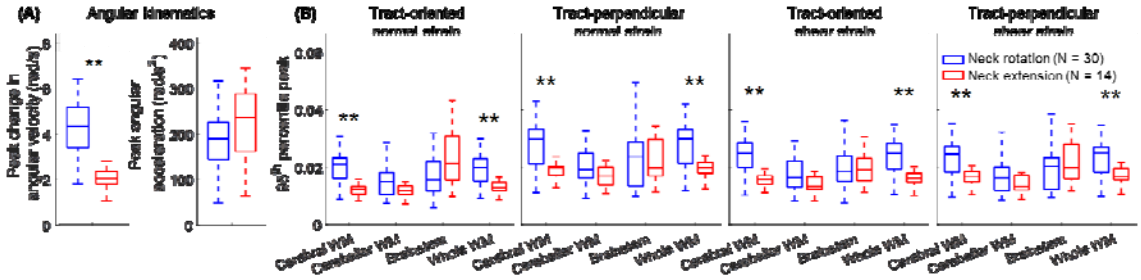

Fig 6. Influence of head loading mode on tract-related strains. (A) Comparisons of peak angular kinematics. (B) Comparison of four tract-related strain peaks (95th percentile values) in cerebral white matter (WM), cerebellar WM, brainstem, and the whole WM between neck rotation and neck extension (**p<0.001, Mann-Whitney U test).

Pearson's correction results between angular kinematics peaks (i.e., peak changes in angular velocity and peak angular acceleration) and maximum tract-related strain peaks (95th percentile values) are summarized in Table 1. The correlation results are mainly dependent on the WM region and head loading mode. For the peak change in angular velocity, significant correlations are noted in cerebral WM and whole WM (all strain types) for neck rotation (Table 1A), and in the brainstem (all strain types) for neck extension (Table 1B). When switching the kinematic parameters to peak angular acceleration, similar correlation results are noted, except that the Person's correlation coefficient values change slightly (Table 1C-D).

Table 1. Person's correlation coefficients between peak angular kinematics (i.e., peak change in angular velocity, peak angular acceleration) and maximum tract-related strains (95th percentile peak) in cerebral white matter (WM), cerebellar WM, brainstem, and whole WM during neck rotation (A, C) and neck extension (B, D). For each loading mode, the significance level is adjusted using the Benjamini-Hochberg method for the correction for multiple comparisons.

Significant correlation
Non-significant correlation

	Pearson's correlation coefficient values Tract-related strains vs. peak change in angular velocity								Pearson's correlation coefficient values Tract-related strains vs. peak angular acceleration							
	(A) Neck rotation (N=30)				(B) Neck extension (N=14)				(C) Neck rotation (N=30)				(D) Neck extension (N=14)			
	Cerebral WM	Cerebellar WM	Brainstem	Whole WM	Cerebral WM	Cerebellar WM	Brainstem	Whole WM	Cerebral WM	Cerebellar WM	Brainstem	Whole WM	Cerebral WM	Cerebellar WM	Brainstem	Whole WM
Tract-oriented normal strain	**0.46**	0.10	0.07	**0.43**	0.14	0.53	**0.67**	0.32	**0.46**	0.15	0.07	**0.43**	0.15	0.51	**0.65**	0.32
Tract-perpendicular normal strain	**0.52**	0.12	-0.02	**0.48**	0.20	0.46	**0.68**	0.31	**0.53**	0.14	0.01	**0.50**	0.19	0.46	**0.67**	0.31
Tract-oriented shear strain	**0.56**	0.17	0.02	**0.52**	0.16	0.60	**0.75**	0.32	**0.57**	0.18	0.01	**0.53**	0.15	0.61	**0.77**	0.31
Tract-perpendicular shear strain	**0.52**	0.12	0.06	**0.49**	0.24	0.48	**0.70**	0.34	**0.53**	0.12	0.08	**0.50**	0.24	0.45	**0.72**	0.33

Discussions

Using the data of 42 volunteer impacts from the open-accessed BBIR dataset,[44,48] the current study estimates *in vivo* WM fiber deformation based on four tract-related strains by relating the brain strain tensor measured by tMRI to fiber orientation estimated from DTI. This multimodal imaging analyses deliver four strain parameters (i.e., tract-oriented normal strain, tract-perpendicular normal strain, tract-oriented shear strain, and tract-perpendicular shear strain), collectively representing a comprehensive description of the fiber deformation. Our work finds the tract-perpendicular normal strain is the largest among the four strain types, unveiling fundamental new aspects of WM dynamics. The reported strain results can be used to evaluate the biofidelity of computational human head models, especially those intended to predict tract-related strains under non-injurious impacts.

The range of tract-related strains in our *in vivo* analyses are generally agreed with the regime in one early *in vivo* measurement of brain strain, and far smaller than the proposed brain injury thresholds from *in silico* studies and the strain magnitude in *in vitro* studies with axonal pathology (Table 2). In 2020, Knutsen and coworkers[48] presented the first *in vivo* measurement of tract-oriented normal strain and reported the range to be 0.007-0.029, largely overlapping with the values in our study (0.009-0.030). *In silico* models have been used to develop brain injury thresholds based on the tract-oriented normal strain. For example, by relating binary injury outcomes (i.e., concussion or no concussion) in sports-related impacts with continuous tract-oriented normal strain data from computational simulations, Giordano and Kleiven[60] proposed an injury threshold of 0.09 for the corpus callosum and 0.15 for the brainstem. Hajiaghamemar and Margulies[29] co-registered the numerically derived tract-oriented normal strain contour with the histology-identified neuropathological map in piglets, reporting the axonal injury threshold fell within the range of 0.08-0.14. Similar thresholds were also developed for diffuse axonal injury in humans (0.15),[61] brain injury in nonhuman primates (0.12 for mild trauma and 0.19 for severe trauma),[62] and impact-induced behavioural changes in rats (0.09).[63] A few *in vitro* studies linked the strain at the cultured tissue to the injury outcome. For example, LaPlaca and colleagues[64] found a significant loss of neurite that occurred at the conditions when the tract-oriented shear strain peaked (~0.56). In another *in vitro* model[65] with neuronal death, the tract-oriented normal and shear strains were within the range of 0.12-0.64 and 0.11-0.48, respectively. Bar-Kochba and coworkers[66] found the axonal bleb formation was strongly correlated with the tract-oriented shear strain with a threshold of 0.14. Nakadate and coworkers[67] found swelling in neurons aligned with and

perpendicular to the loading direction (a strain of 0.22 at a strain rate of 37 /s). Braun and coworks[68] also observed tau pathology in neurons oriented along and perpendicular to the loading direction at the strain magnitudes of 0.05 and 0.20, respectively. It should be clarified that the scale of interest may not necessarily be the same between the *in vitro* studies (axon/neuron level) and the current work (fiber tract level). Taken together, the tract-related strain values in *in silico* and *in vitro* studies with varying injury outcomes largely exceed the range in our study under *in vivo* volunteer impacts.

Table 2. Comparison of tract-related strains among *in vivo*, *in silico*, and *in vitro* studies. Note that the nomenclature in the listed studies may not be the same and are converted to the one in the current study. For the three superscripts, [a]: the values are estimated from Fig 7 of the cited reference; [b]: the values are estimated from Fig 4 of the cited reference; [c]: the values are estimated from Fig 9 of the cited reference; [d]: In the original article, the value was averaged along the length of the neuron; [e]: the values are obtained based on the assumption that the strain levels in the embedded neuron are the same as those imposed to the cultured experimental tissue.

Reference		*Peak angular acceleration (rad/s^2)*		*Tract-oriented normal strain*	*Tract-perpendicular normal strain*	*Tract-oriented shear strain*	*Tract-perpendicular shear strain*
In vivo	Current study	Neck rotation (N=30)	185.5 ± 59.2	0.009-0.030	0.011-0.042	0.010-0.035	0.010-0.035
		Neck extension (N=14)	228.6 ± 8.3	0.009-0.017	0.012-0.024	0.010-0.020	0.011-0.022
	Knutsen and coworkers[48]	Neck rotation (N=10)	212.8 ± 32.1	0.007-0.024[a]			
		Neck extension (N=10)	282.8 ± 47.4	0.008-0.029[a]			
Reference		*Thresholds of 50% injury risk*		*Tract-oriented normal strain*	*Tract-perpendicular normal strain*	*Tract-oriented shear strain*	*Tract-perpendicular shear strain*
In silico	Giordano and Kleiven[60]	Concussion (human)		0.07-0.15			
	Sahoo and colleagues[61]	Diffuse axonal injury (human)		0.15			
	Wu and colleagues[62]	Brain injury (primate)		0.12-0.19			
	Hajiaghamemar and Margulies[29]	Diffuse axonal injury (pig)		0.08-0.14			
	Premi and colleagues[63]	Behavioural alteration (rat)		0.09			
Reference		*Injury pathology*		*Tract-oriented normal strain*	*Tract-perpendicular normal strain*	*Tract-oriented shear strain*	*Tract-perpendicular shear strain*
In vitro	LaPlaca and coworkers[64]	Neurite loss				~0.56[b]	
	Cullen and LaPlaca[65]	Neuron death		~0.12-0.64[c]		~0.11-0.48[c]	
	Bar-Kochba and coworkers[66]	Neuron bleb formation				0.14[d]	
	Nakadate and coworkers[67]	Neuron swelling		0.22[e]	0.22[e]		
	Braun and coworks[68]	Tau mislocalization		0.05[e]	0.2[e]		

Our work unravels the WM fiber tract deforms most in normal in the perpendicular direction, holding significant implications for brain injury mechanics. At present, the stretch along the fiber direction is widely recognized as the pathogenesis of axonal injury, as substantiated by the growing body of literature that employs tract-oriented normal strain as an axonal injury criterion.[47,60-62,69,70] Indeed, several *in vitro* studies reported under the same magnitude level, the tract-oriented normal strain instigated more severe axonal pathology than the tract-perpendicular normal strain,[67,68] indicating a higher tolerance level for the normal strain perpendicular to the neurites. However, our work finds that under *in vivo* human head impacts, the tract-perpendicular normal strain is significantly larger than the tract-oriented normal strain. Thereby, one cannot exclude the possibility

that the tract-perpendicular strain is one possible instigator of axonal pathology in real-world impacts. When switching to the shear strain, *in vitro* studies also observed neurite loss and neuron death in the regime when the tract-oriented shear strain peaked.[64,65] Taken together, it can be concluded that the existing brain injury investigation may have neglected important aspects of axonal pathogenesis.

The larger value of tract-perpendicular strain than its counterparts under volunteer tests may be attributed to the anisotropic material property of WM. Of particular relevance, several *in vivo* studies on the human[71,72] and the minipig[73,74] analyzed the wave motion fields measured by MRE using transversely isotropic nonlinear inversion algorithms and found that the tensile stiffness perpendicular to the fiber tract was lower than that parallel to the fiber tract. Similar findings have also been reported in several *in vitro* brain tissue material tests.[75-79] The mechanical reinforcement along the fiber direction provides a possible explanation for why the fiber tract deforms more in the perpendicular direction than the normal direction. However, it should be noted that no consensus has been reached yet about brain anisotropy as another body of literature reported that no significant mechanical dependency on WM fiber orientation was noted in the brain tissue.[80-83] Another potential explanation for disproportional magnitudes of tract-related strains is related to the feature of strain tensor. For the tract-oriented normal strain, its magnitude is constant across the tract-aligned coordinate system with one axis aligned with the fiber direction. In contrast, the magnitude of the tract-perpendicular strain changes when the coordinate system rotates around the fiber direction and its maximum value across all tract-aligned coordinate systems is presented in the current study, corresponding to the most severe loading scenario (Appendix A).

Our results also find laterally symmetric strain patterns with respect to the midsagittal plane under neck extensions, but not under neck rotations (Figs 3-4). This can be explained by the presence of cerebral falx at the interhemispheric fissure with mechanically stiffer properties than the brain (i.e., ~ 22.9 MPa for the elastic moduli of falx[84] vs. ~ 1 kPa level for the shear stiffness of the brain).[85] During neck extensions, the brain primarily moves within the sagittal plane (confirmed by the displacement field recorded by tMRI) with little interaction with the anterior-posterior oriented falx, and hence left-right symmetric deformation patterns are developed in the brain. Under neck rotations, the primary brain displacement is noted within the coronal plane. The presence of the mechanically stiffer falx disturbs the brain motion, leading to asymmetric strain patterns. Similar findings have been reported in earlier *in vivo* imaging studies[38,48] and *in silico* impact simulations.[86,87] Collectively, these studies highlight the mechanical role of the falx during impacts.

Our study represents a significant extension of one early *in vivo* tract-oriented normal strain estimation (10 neck rotations and 10 neck extensions)[48] by involving more impacts (30 neck rotations and 14 neck extensions). Except for the overlap of the tract-oriented normal strain ranges described above, both our work and the early study[48] found high tract-oriented normal strains primarily in the cerebral WM for neck rotations and in the brainstem for neck extensions (Fig 3), providing

independent verification of each other. Moreover, we generate spatially detailed information on how the axonal fiber responds to normal strain perpendicular to the fiber tract and shear strain along and perpendicular to the fiber tract, representing three new aspects of fiber deformation. Knutsen and coworkers[48] found the square of angular velocity peak strongly correlated with the maximum tract-oriented normal strain in the corpus callosum during neck rotations and in the brainstem during neck extensions. Here, we expand the correlation by incorporating other kinematic-based metrics (i.e., peak change in angular velocity and peak angular acceleration) and four tract-related strains, through which we find both angular kinematics-based peaks significantly correlated with the tract-related strains (all four types) in cerebral WM and whole WM for neck rotations, and in the brainstem (all four types) for neck extensions (Table 1). To provide further verification of the observed relationships, in-house *in silico* work is ongoing to extend the correlation analyses by including impacts with higher severities.[88]

The current work provides important data for the validation of computational head models. Partially owing to the development of numerical algorithms (e.g., finite element method and material point method), computational head models have become increasingly used to study brain biomechanics.[16] Prior to the utilization, the reliability of computational head models requires to be extensively evaluated against relevant experimental measurements. Existing head models are often validated against cadaveric measurements in the form of brain-skull relative motion[7,11,89], maximum principal and shear strain,[8,9] and maximum principal strain rate[10] from only a handful of intracranial sites with the impact severities close to traumatic levels. Despite the great value of cadaveric tests, the material property of the brain changes after death. This is further complicated by the influence of post-mortem time and storage conditions without consensuses being reached yet.[85] One possible solution is to validate the model's responses collectively against the measurements from high-severity, sparsely recorded cadaveric experiments and low-severity, spatially detailed volunteer tests (such as the brain strain data presented herein). This may be particularly relevant for those models with intended usage to predict the brain response under non-injurious impacts. Emerging attempts have been noted in validating the computational head model against *in vivo* brain responses in the form of brain-skull relative displacement,[90] maximum principal strain,[22,23,87,91] maximum shear strain,[87] and tract-oriented normal strain.[22,23] Our study computes 3D normal and shear strains along and perpendicular to the fiber tract (spatial resolution: 1.5 mm or 2 mm, temporal resolution: 18 ms, 19.5 ms, or 20 ms) across the whole WM from 44 volunteer impacts. These strain data are complementary to the existing cadaveric experiments. Collectively, these *in vivo* and *in situ* experimental data may contribute to the validation of computational brain models towards a comprehensive degree and ensure the confidence of model usage to estimate brain response across the sub-injurious and injurious levels.

As motivated by the prevalence choice of using normal and shear strain (e.g., maximum principal strain, maximum shear strain) for brain injury analysis,[92] the current study presents the normal strain and shear strain along and perpendicular to fiber tracts. Recent trends were noted in employing the

compressive normal strain as the parameter of interest, e.g., minimum principal strain,[93-95] compressive strain at the fiber tract level,[96] neuronal level,[66] and microtube level.[97] For example, two *in vitro* studies imposed compressive normal strains perpendicular to the main axonal direction and found cytoskeletal degeneration (e.g., changes in neurofilament and microtube distributions),[98,99] suggesting the tract-perpendicular normal strain in compression as another possible trigger of axonal injury. In relation to our study, the tract-perpendicular normal strain at a given time instance may attain both positive value (i.e., tensile strain) and negative value (i.e., compressive strain) with dependency on the choice of coordinate systems (see equations 3-4 in Appendix A). Although the current study focuses on the tensile normal strain (e.g., $\varepsilon_t^{\max}$ represents the maximum tract-perpendicular normal strain, see Appendix A), we also present the equation for computing the minimum tract-perpendicular strain across all tract-aligned coordinate systems (see $\varepsilon_t^{\min}$ in Appendix A). Other researchers, who are interested in computing the compressive normal strain perpendicular to the fiber tract, may find this equation helpful.

The current study is based on volunteer tests and imaging data from the open-access BBIR dataset. Despite its great value, the dataset suffers certain limitations (e.g, varying resolutions in the temporal and spatial domains between different tests) that were already detailed by the dataset developer.[44] Other challenges and caveats, e.g., the limited number of image frames in tMRI,[41,48] the adverse effect of decreased signal-to-noise ratio on strain estimation as tag lines fade,[100] incapability of diffusion tensor to describe the region of crossing fibers with multiple orientations present within the voxel,[48,101,102] are exhaustively discussed elsewhere and not reiterated herein.

Conclusion

Based on the volunteer impact data from the BBIR dataset,[44,48] this study calculates WM tract-related deformation during voluntary impacts by relating the tMRI-recorded brain strain tensor to DTI-derived fiber orientation through coordinate transformation. By extending the previous effort that focused on the normal strain along the fiber tract, we present *in vivo* data of the normal strain perpendicular to the fiber tract and shear strain along and perpendicular to the fiber tract towards a multifaceted understanding of WM dynamics. Our work finds the fiber tract deforms most in the perpendicular direction, deciphering new fundamentals of brain biomechanics. The reported strain results under volunteer impacts can be used to evaluate the fidelity of computational head models, especially those intended to predict fiber deformation under non-injurious conditions.

Transparency, Rigor, and Reproducibility

The *in vivo* imaging data used for the computation of white matter fiber deformation are obtained from an open-access dataset (see the acknowledgements). The rigor and reproducibility are ensured by the steps for the calculation of four tract-related strains and statistical analyses presented in the paper.

The yielded strain maps, including 4 tract-related strains from 44 impacts, can be requested by emailing request to the corresponding author.

Funding statement

This research has received funding from KTH Royal Institute of Technology (Stockholm, Sweden), the Swedish Governmental Agency for Innovation systems (VINNOVA) (no. 2023-00753), Swedish Research Council (VR-2020-04496 and VR-2020-04724), Skyltfonden from the trafiksäkerhet (TRV 2024/23811), and the Torvald and Britta Gahlin's foundation.

Acknowledgements

Data were provided in part by the Brain Biomechanics Imaging Repository (http://www.nitrc.org/projects/bbir). Principal Investigators: P. Bayly, D. Pham, C. Johnson, J. Prince, K. Ramesh, through grants U01 NS11212 and R56 NS055951. The content of this article is solely the responsibility of the authors and does not necessarily represent the official views of neither funding agencies nor the dataset developer. The computation of tract-related strains was enabled by resources provided by the National Academic Infrastructure for Supercomputing in Sweden (NAISS) at the center for High Performance Computing (PDC) partially funded by the Swedish Research Council through grant agreement no. 2022-06725.

Conflict of Interest

The authors declare that they have no conflict of interest.

Author contribution

Zhou Zhou: Conceptualization, Formal analysis, Funding acquisition, Methodology, Software, Visualization, Original draft, Review & editing. **Christoffer Olsson**: Conception and study design, Investigation, Software, Review & editing. **T. Christian Gasser**: Formal analysis, Investigation, Methodology, Original draft, Review & editing. **Xiaogai Li**: Visualization, Methodology, Review & editing. **Svein Kleiven**: Methodology, Original draft, Review & editing, Funding acquisition.

References

1. Dewan MC, Rattani A, Gupta S, et al. Estimating the global incidence of traumatic brain injury. Journal of neurosurgery 2018;130(4):1080-1097
2. Brazinova A, Rehorcikova V, Taylor MS, et al. Epidemiology of traumatic brain injury in Europe: a living systematic review. Journal of neurotrauma 2021;38(10):1411-1440
3. Pedersen K, Fahlstedt M, Jacobsson A, et al. A national survey of traumatic brain injuries admitted to hospitals in Sweden from 1987 to 2010. Neuroepidemiology 2015;45(1):20-27
4. Maas AI, Menon DK, Manley GT, et al. Traumatic brain injury: progress and challenges in prevention, clinical care, and research. The Lancet Neurology 2022;21(11):1004-1060

5. Alshareef A, Giudice J, Shedd D, et al. Experimental data for validating the structural response of computational brain models. In: Multiscale Biomechanical Modeling of the Brain. Elsevier: 2022; pp. 193-208.
6. Hardy WN. Response of the human cadaver head to impact. Wayne State University: 2007.
7. Hardy WN, Mason MJ, Foster CD, et al. A study of the response of the human cadaver head to impact. Stapp car crash journal 2007;51(17-80
8. Zhou Z, Li X, Kleiven S, et al. Brain Strain from Motion of Sparse Markers. Stapp car crash journal 2019;63(1-27
9. Zhou Z, Li X, Kleiven S, et al. A Reanalysis of Experimental Brain Strain Data: Implication for Finite Element Head Model Validation. Stapp car Crash Journal 2018;62(293-318
10. Zhou Z, Li X, Liu Y, et al. Brain strain rate response: addressing computational ambiguity and experimental data for model validation. Brain Multiphysics 2023;4(100073
11. Alshareef A, Giudice JS, Forman J, et al. Biomechanics of the human brain during dynamic rotation of the head. Journal of neurotrauma 2020;37(13):1546-1555
12. Morrison III B, Elkin BS, Dollé J-P, et al. In vitro models of traumatic brain injury. Annual review of biomedical engineering 2011;13(91-126
13. Wu Y-H, Rosset S, Lee T-r, et al. In vitro models of traumatic brain injury: A systematic review. Journal of Neurotrauma 2021;38(17):2336-2372
14. Cater HL, Sundstrom LE, Morrison III B. Temporal development of hippocampal cell death is dependent on tissue strain but not strain rate. Journal of biomechanics 2006;39(15):2810-2818
15. Kang WH, Morrison III B. Functional tolerance to mechanical deformation developed from organotypic hippocampal slice cultures. Biomechanics and modeling in mechanobiology 2015;14(3):561-575
16. Ji S, Ghajari M, Mao H, et al. Use of brain biomechanical models for monitoring impact exposure in contact sports. Annals of Biomedical Engineering 2022;50(11):1389-1408
17. Madhukar A, Ostoja-Starzewski M. Finite element methods in human head impact simulations: a review. Annals of biomedical engineering 2019;47(1832-1854
18. Li X, Zhou Z, Kleiven S. An anatomically detailed and personalizable head injury model: Significance of brain and white matter tract morphological variability on strain. Biomechanics and modeling in mechanobiology 2021;20(403-431
19. Giudice JS, Alshareef A, Wu T, et al. An image registration-based morphing technique for generating subject-specific brain finite element models. Annals of Biomedical Engineering 2020;48(2412-2424
20. Li X. Subject-specific head model generation by mesh morphing: a personalization framework and its applications. Frontiers in bioengineering and biotechnology 2021;9(706566
21. Giordano C, Cloots R, Van Dommelen J, et al. The influence of anisotropy on brain injury prediction. Journal of biomechanics 2014;47(5):1052-1059
22. Alshareef A, Knutsen AK, Johnson CL, et al. Integrating material properties from magnetic resonance elastography into subject-specific computational models for the human brain. Brain multiphysics 2021;2(100038
23. Upadhyay K, Alshareef A, Knutsen AK, et al. Development and validation of subject-specific 3D human head models based on a nonlinear visco-hyperelastic constitutive framework. Journal of the Royal Society Interface 2022;19(195):20220561
24. Zhou Z, Li X, Kleiven S. Fluid–structure interaction simulation of the brain–skull interface for acute subdural haematoma prediction. Biomechanics and modeling in mechanobiology 2019;18(155-173
25. Zhou Z, Li X, Kleiven S. Evaluation of brain-skull interface modelling approaches on the prediction of acute subdural hematoma in the elderly. Journal of biomechanics 2020;105(109787
26. Zhou Z, Li X, Kleiven S. Biomechanics of periventricular injury. Journal of neurotrauma 2020;
27. Montanino A, Li X, Zhou Z, et al. Subject-specific multiscale analysis of concussion: from macroscopic loads to molecular-level damage. Brain multiphysics 2021;2(100027
28. Yuan Q, Li X, Zhou Z, et al. A novel framework for video-informed reconstructions of sports accidents: A case study correlating brain injury pattern from multimodal neuroimaging with finite element analysis. Brain Multiphysics 2024;6(100085

29. Hajiaghamemar M, Margulies SS. Multi-scale white matter tract embedded brain finite element model predicts the location of traumatic diffuse axonal injury. Journal of Neurotrauma 2021;38(1):144-157
30. Zhang C, Bartels L, Clansey A, et al. A computational pipeline towards large-scale and multiscale modeling of traumatic axonal injury. Computers in Biology and Medicine 2024;108109
31. Bayly PV, Clayton EH, Genin GM. Quantitative imaging methods for the development and validation of brain biomechanics models. Annual review of biomedical engineering 2012;14(369-396
32. McCracken PJ, Manduca A, Felmlee J, et al. Mechanical transient-based magnetic resonance elastography. Magnetic Resonance in Medicine 2005;53(3):628-639, doi:https://doi.org/10.1002/mrm.20388
33. Muthupillai R, Lomas D, Rossman P, et al. Magnetic resonance elastography by direct visualization of propagating acoustic strain waves. science 1995;269(5232):1854-1857
34. Abderezaei J, Pionteck A, Terem I, et al. Development, calibration, and testing of 3D amplified MRI (aMRI) for the quantification of intrinsic brain motion. Brain Multiphysics 2021;2(100022
35. Reese TG, Feinberg DA, Dou J, et al. Phase contrast MRI of myocardial 3D strain by encoding contiguous slices in a single shot. Magnetic Resonance in Medicine: An Official Journal of the International Society for Magnetic Resonance in Medicine 2002;47(4):665-676
36. Zerhouni EA, Parish DM, Rogers WJ, et al. Human heart: tagging with MR imaging--a method for noninvasive assessment of myocardial motion. Radiology 1988;169(1):59-63
37. Bayly PV, Cohen T, Leister E, et al. Deformation of the human brain induced by mild acceleration. Journal of neurotrauma 2005;22(8):845-856
38. Sabet AA, Christoforou E, Zatlin B, et al. Deformation of the human brain induced by mild angular head acceleration. Journal of biomechanics 2008;41(2):307-315
39. Feng Y, Abney TM, Okamoto RJ, et al. Relative brain displacement and deformation during constrained mild frontal head impact. Journal of the Royal Society Interface 2010;7(53):1677-1688
40. Knutsen AK, Magrath E, McEntee JE, et al. Improved measurement of brain deformation during mild head acceleration using a novel tagged MRI sequence. Journal of biomechanics 2014;47(14):3475-3481
41. Gomez AD, Knutsen AK, Xing F, et al. 3-D measurements of acceleration-induced brain deformation via harmonic phase analysis and finite-element models. IEEE Transactions on Biomedical Engineering 2018;66(5):1456-1467
42. Xing F, Woo J, Gomez AD, et al. Phase vector incompressible registration algorithm for motion estimation from tagged magnetic resonance images. IEEE transactions on medical imaging 2017;36(10):2116-2128
43. Chan DD, Knutsen AK, Lu Y-C, et al. Statistical characterization of human brain deformation during mild angular acceleration measured in vivo by tagged magnetic resonance imaging. Journal of biomechanical engineering 2018;140(10):101005
44. Bayly PV, Alshareef A, Knutsen AK, et al. MR imaging of human brain mechanics in vivo: new measurements to facilitate the development of computational models of brain injury. Annals of biomedical engineering 2021;49(2677-2692
45. Maxwell WL, Povlishock JT, Graham DL. A mechanistic analysis of nondisruptive axonal injury: a review. Journal of neurotrauma 1997;14(7):419-440
46. Povlishock JT. Traumatically induced axonal injury: pathogenesis and pathobiological implications. Brain pathology 1991;2(1):1-12
47. Wright RM, Post A, Hoshizaki B, et al. A multiscale computational approach to estimating axonal damage under inertial loading of the head. Journal of neurotrauma 2013;30(2):102-118
48. Knutsen AK, Gomez AD, Gangolli M, et al. In vivo estimates of axonal stretch and 3D brain deformation during mild head impact. Brain multiphysics 2020;1(100015
49. Ji S, Zhao W, Ford JC, et al. Group-wise evaluation and comparison of white matter fiber strain and maximum principal strain in sports-related concussion. Journal of neurotrauma 2015;32(7):441-454
50. Sullivan S, Eucker SA, Gabrieli D, et al. White matter tract-oriented deformation predicts traumatic axonal brain injury and reveals rotational direction-specific vulnerabilities. Biomechanics and modeling in mechanobiology 2015;14(877-896

51. Zhou Z, Li X, Liu Y, et al. Toward a comprehensive delineation of white matter tract-related deformation. Journal of neurotrauma 2021;38(23):3260-3278
52. Zhou Z, Domel AG, Li X, et al. White matter tract-oriented deformation is dependent on real-time axonal fiber orientation. Journal of neurotrauma 2021;38(12):1730-1745
53. Carlsen RW, Fawzi AL, Wan Y, et al. A quantitative relationship between rotational head kinematics and brain tissue strain from a 2-D parametric finite element analysis. Brain Multiphysics 2021;2(100024
54. Le Bihan D, Mangin JF, Poupon C, et al. Diffusion tensor imaging: concepts and applications. Journal of Magnetic Resonance Imaging: An Official Journal of the International Society for Magnetic Resonance in Medicine 2001;13(4):534-546
55. Jenkinson M, Bannister P, Brady M, et al. Improved optimization for the robust and accurate linear registration and motion correction of brain images. Neuroimage 2002;17(2):825-841
56. Jenkinson M, Smith S. A global optimisation method for robust affine registration of brain images. Medical image analysis 2001;5(2):143-156
57. Zhan X, Li Y, Liu Y, et al. Predictive factors of kinematics in traumatic brain injury from head impacts based on statistical interpretation. Annals of biomedical engineering 2021;49(2901-2913
58. Huber CM, Patton DA, Maheshwari J, et al. Finite element brain deformation in adolescent soccer heading. Computer methods in biomechanics and biomedical engineering 2023;1-11
59. Zhou Z, Li X, Domel AG, et al. The presence of the temporal horn exacerbates the vulnerability of hippocampus during head impacts. Frontiers in Bioengineering and Biotechnology 2022;10(754344
60. Giordano C, Kleiven S. Evaluation of Axonal Strain as a Predictor for Mild Traumatic Brain Injuries Using Finite Element Modeling. Stapp car Crash Journal 2014;58(29-61
61. Sahoo D, Deck C, Willinger R. Brain injury tolerance limit based on computation of axonal strain. Accident Analysis & Prevention 2016;92(53-70
62. Wu T, Hajiaghamemar M, Giudice JS, et al. Evaluation of tissue-level brain injury metrics using species-specific simulations. Journal of neurotrauma 2021;38(13):1879-1888
63. Premi S, Deck C, Stemper BD, et al. Mechanical threshold for concussion based on computation of axonal strain using a finite element rat brain model. Brain Multiphysics 2021;2(100032
64. LaPlaca MC, Cullen DK, McLoughlin JJ, et al. High rate shear strain of three-dimensional neural cell cultures: a new in vitro traumatic brain injury model. Journal of biomechanics 2005;38(5):1093-1105
65. Cullen DK, LaPlaca MC. Neuronal response to high rate shear deformation depends on heterogeneity of the local strain field. Journal of neurotrauma 2006;23(9):1304-1319
66. Bar-Kochba E, Scimone MT, Estrada JB, et al. Strain and rate-dependent neuronal injury in a 3D in vitro compression model of traumatic brain injury. Scientific reports 2016;6(1):30550
67. Nakadate H, Kurtoglu E, Furukawa H, et al. Strain-Rate Dependency of Axonal Tolerance for Uniaxial Stretching. Stapp car Crash Journal 2017;61(53-65
68. Braun NJ, Liao D, Alford PW. Orientation of neurites influences severity of mechanically induced tau pathology. Biophysical journal 2021;120(16):3272-3282
69. Zhao W, Cai Y, Li Z, et al. Injury prediction and vulnerability assessment using strain and susceptibility measures of the deep white matter. Biomechanics and modeling in mechanobiology 2017;16(1709-1727
70. Wu T, Antona-Makoshi J, Alshareef A, et al. Investigation of cross-species scaling methods for traumatic brain injury using finite element analysis. Journal of neurotrauma 2020;37(2):410-422
71. Smith DR, Caban-Rivera DA, McGarry MD, et al. Anisotropic mechanical properties in the healthy human brain estimated with multi-excitation transversely isotropic MR elastography. Brain multiphysics 2022;3(100051
72. Caban-Rivera DA, Williams LT, McGarry MD, et al. Mechanical Properties of White Matter Tracts in Aging Assessed via Anisotropic MR Elastography. bioRxiv 2024;2024.05. 08.593260
73. Wang S, Guertler CA, Okamoto RJ, et al. Mechanical stiffness and anisotropy measured by MRE during brain development in the minipig. NeuroImage 2023;277(120234
74. Wang S, Eckstein KN, Guertler CA, et al. Post-Mortem Changes of Anisotropic Mechanical Properties in the Porcine Brain Assessed by MR Elastography. Brain Multiphysics 2024;100091
75. Arbogast KB, Margulies SS. A fiber-reinforced composite model of the viscoelastic behavior of the brainstem in shear. Journal of biomechanics 1999;32(8):865-870

76. Feng Y, Okamoto RJ, Namani R, et al. Measurements of mechanical anisotropy in brain tissue and implications for transversely isotropic material models of white matter. Journal of the mechanical behavior of biomedical materials 2013;23(117-132
77. Jin X, Zhu F, Mao H, et al. A comprehensive experimental study on material properties of human brain tissue. Journal of biomechanics 2013;46(16):2795-2801
78. Prange MT, Margulies SS. Regional, directional, and age-dependent properties of the brain undergoing large deformation. J Biomech Eng 2002;124(2):244-252
79. Velardi F, Fraternali F, Angelillo M. Anisotropic constitutive equations and experimental tensile behavior of brain tissue. Biomechanics and modeling in mechanobiology 2006;5(1):53-61
80. Budday S, Sommer G, Birkl C, et al. Mechanical characterization of human brain tissue. Acta biomaterialia 2017;48(319-340
81. MacManus DB, Pierrat B, Murphy JG, et al. Region and species dependent mechanical properties of adolescent and young adult brain tissue. Scientific reports 2017;7(1):13729
82. Pervin F, Chen WW. Dynamic mechanical response of bovine gray matter and white matter brain tissues under compression. Journal of biomechanics 2009;42(6):731-735
83. Shuck L, Advani S. Rheological response of human brain tissue in shear. Journal of Basic Engineering 1972;94(4):905-911
84. Walsh DR, Ross AM, Newport DT, et al. Mechanical characterisation of the human dura mater, falx cerebri and superior sagittal sinus. Acta Biomaterialia 2021;134(388-400
85. Budday S, Ovaert TC, Holzapfel GA, et al. Fifty shades of brain: a review on the mechanical testing and modeling of brain tissue. Archives of Computational Methods in Engineering 2020;27(1187-1230
86. Ho J, Zhou Z, Li X, et al. The peculiar properties of the falx and tentorium in brain injury biomechanics. Journal of biomechanics 2017;60(243-247
87. Lu Y-C, Daphalapurkar NP, Knutsen A, et al. A 3D computational head model under dynamic head rotation and head extension validated using live human brain data, including the falx and the tentorium. Annals of biomedical engineering 2019;47(1923-1940
88. Zhou Z, Fahlstedt M, Li X, et al. Peaks and Distributions of White Matter Tract-related Strains in Bicycle Helmeted Impacts: Implication for Helmet Ranking and Optimization. bioRxiv 2024;2024.04. 26.591318
89. Hardy W, Foster C, Mason M, et al. Investigation of Head Injury Mechanisms Using Neutral Density Technology and High-Speed Biplanar X-ray. Stapp car Crash Journal 2001;45(337-368
90. Hernandez F, Giordano C, Goubran M, et al. Lateral impacts correlate with falx cerebri displacement and corpus callosum trauma in sports-related concussions. Biomechanics and modeling in mechanobiology 2019;18(631-649
91. Zhao W, Ji S. Displacement-and strain-based discrimination of head injury models across a wide range of blunt conditions. Annals of biomedical engineering 2020;48(1661-1677
92. Rowson B, Duma SM. A review of head injury metrics used in automotive safety and sports protective equipment. Journal of biomechanical engineering 2022;144(11):110801
93. Miller LE, Urban JE, Davenport EM, et al. Brain strain: computational model-based metrics for head impact exposure and injury correlation. Annals of biomedical engineering 2021;49(1083-1096
94. Ji S, Wu S, Zhao W. Dynamic characteristics of impact-induced brain strain in the corpus callosum. Brain Multiphysics 2022;3(100046
95. Bradfield C, Voo L, Drewry III D, et al. Dynamic strain fields of the mouse brain during rotation. Biomechanics and Modeling in Mechanobiology 2023;1-16
96. Garimella HT, Kraft RH. Modeling the mechanics of axonal fiber tracts using the embedded finite element method. International journal for numerical methods in biomedical engineering 2017;33(5):e2823
97. Soheilypour M, Peyro M, Peter SJ, et al. Buckling behavior of individual and bundled microtubules. Biophysical journal 2015;108(7):1718-1726
98. Fournier AJ, Hogan JD, Rajbhandari L, et al. Changes in neurofilament and microtubule distribution following focal axon compression. PloS one 2015;10(6):e0131617
99. Fournier AJ, Rajbhandari L, Shrestha S, et al. In vitro and in situ visualization of cytoskeletal deformation under load: traumatic axonal injury. The FASEB Journal 2014;28(12):5277-5287

100. Bian Z, Alshareef A, Wei S, et al. Is Registering Raw Tagged-MR Enough for Strain Estimation in the Era of Deep Learning? arXiv preprint arXiv:240117571 2024;
101. Jeurissen B, Leemans A, Tournier JD, et al. Investigating the prevalence of complex fiber configurations in white matter tissue with diffusion magnetic resonance imaging. Human brain mapping 2013;34(11):2747-2766
102. Zhou Z, Wang T, Jörgens D, et al. Fiber orientation downsampling compromises the computation of white matter tract-related deformation. journal of the mechanical behavior of biomedical materials 2022;132(105294
103. Scimone MT, Cramer III HC, Bar-Kochba E, et al. Modular approach for resolving and mapping complex neural and other cellular structures and their associated deformation fields in three dimensions. Nature protocols 2018;13(12):3042-3064

Appendix A Computation of tract-related strains

At a given time instance, the white matter (WM) tract-related strains are calculated by transforming the brain strain tensor to the coordinate system with one axis aligned with the fiber orientation. For a WM voxel (i.e., voxel with the fractional anisotropy value ≥0.2), the primary fiber orientation is approximated as the first principal eigenvector of diffusion tensor (denoted as $\boldsymbol{v} = [v_1 \quad v_2 \quad v_3]^{\mathrm{T}}$). At each time frame, the brain strain tensor $\boldsymbol{E}_{\mathrm{global}}$ in tMRI (Fig 1D) is expressed with reference to the global coordinate system ($\boldsymbol{XYZ}$, $\boldsymbol{X} = [1 \quad 0 \quad 0]^{\mathrm{T}}$, $\boldsymbol{Y} = [0 \quad 1 \quad 0]^{\mathrm{T}}$, $\boldsymbol{Z} = [0 \quad 0 \quad 1]^{\mathrm{T}}$, Fig A1A). We rotate $\boldsymbol{E}_{\mathrm{global}}$ into the local coordinate system (1) ($\boldsymbol{xyz}$ in Fig A1B, $\boldsymbol{x}$ is aligned with $\boldsymbol{v}$, $\boldsymbol{y}$ is the cross product of $\boldsymbol{x}$ and $\boldsymbol{X}$, $\boldsymbol{z}$ is the cross product of $\boldsymbol{x}$ and $\boldsymbol{y}$) via $\boldsymbol{E}_{\mathrm{tract}} = \boldsymbol{Q}\boldsymbol{E}_{\mathrm{global}}\boldsymbol{Q}^{\mathrm{T}}$, in which

$$\boldsymbol{Q} = \begin{bmatrix} \cos(\boldsymbol{x},\boldsymbol{X}) & \cos(\boldsymbol{x},\boldsymbol{Y}) & \cos(\boldsymbol{x},\boldsymbol{Z}) \\ \cos(\boldsymbol{y},\boldsymbol{X}) & \cos(\boldsymbol{y},\boldsymbol{Y}) & \cos(\boldsymbol{y},\boldsymbol{Z}) \\ \cos(\boldsymbol{z},\boldsymbol{X}) & \cos(\boldsymbol{z},\boldsymbol{Y}) & \cos(\boldsymbol{z},\boldsymbol{Z}) \end{bmatrix} = \begin{bmatrix} v_1 & v_2 & v_3 \\ 0 & \dfrac{-v_3}{\sqrt{(v_2^2+v_3^2)}} & \dfrac{v_2}{\sqrt{(v_2^2+v_3^2)}} \\ \sqrt{(v_2^2+v_3^2)} & \dfrac{-v_1 v_2}{\sqrt{(v_2^2+v_3^2)}} & \dfrac{-v_1 v_3}{\sqrt{(v_2^2+v_3^2)}} \end{bmatrix} \tag{1}$$

The six independent strain components in the local coordinate system (1) are illustrated in Fig A1C.

With respect to strain components ε_{xx}, γ_{xy}, and γ_{xz} (the latter two act at the plane perpendicular to the fiber direction, i.e., yz plane, see Fig A1D), we form two strain measures, i.e., the tract-oriented normal strain $\varepsilon_a = \varepsilon_{xx}$ represents the normal strain along the fiber tract (Fig A1E), and the shear strain $\gamma_a = \sqrt{\gamma_{xy}^2 + \gamma_{xz}^2}$ within the yz plane. Given the symmetry of the strain tensor, γ_a also appears along the fiber and it therefore denotes the tract-oriented shear strain (Fig A1E).

Now we consider the strain components ε_{yy}, ε_{zz}, and γ_{yz}, acting on the xy and xz planes (Fig A1C). Rotating these planes around the fiber direction changes the values of the individual strain

components (i.e., $\boldsymbol{E}_{\text{tract}(i)} = \boldsymbol{Q}_{\theta_i} \boldsymbol{E}_{\text{tract}} \boldsymbol{Q}_{\theta_i}^{\text{T}}$ in the local coordinate system (i) ($\boldsymbol{x}\boldsymbol{y}_i\boldsymbol{z}_i$)) with dependency on the rotating angle ($0^\circ \le \theta_i \le 360^\circ$) (see Fig 5B). Note that,

$$\boldsymbol{Q}_{\theta_i} = \begin{bmatrix} \cos(\boldsymbol{x},\boldsymbol{x}) & \cos(\boldsymbol{x},\boldsymbol{y}) & \cos(\boldsymbol{x},\boldsymbol{z}) \\ \cos(\boldsymbol{y}_i,\boldsymbol{x}) & \cos(\boldsymbol{y}_i,\boldsymbol{y}) & \cos(\boldsymbol{y}_i,\boldsymbol{z}) \\ \cos(\boldsymbol{z}_i,\boldsymbol{x}) & \cos(z_i,\boldsymbol{y}) & \cos(\boldsymbol{z}_i,\boldsymbol{z}) \end{bmatrix} = \begin{bmatrix} 1 & 0 & 0 \\ 0 & \cos\theta_i & -\sin\theta_i \\ 0 & \sin\theta_i & \cos\theta_i \end{bmatrix} \tag{2}$$

The equations for the strain components ε_{yy}, ε_{zz}, and γ_{yz} in $\boldsymbol{E}_{\text{tract}(i)}$ are

$$\varepsilon_{y_i y_i}(\theta_i) = \frac{\varepsilon_{yy} + \varepsilon_{zz}}{2} - \sqrt{(\frac{\varepsilon_{yy} - \varepsilon_{zz}}{2})^2 + \gamma_{yz}^2}\,\sin(2\theta_i + \varphi_1)\ (\varphi_1 = \arctan(\frac{\varepsilon_{yy} - \varepsilon_{zz}}{2\gamma_{yz}})) \tag{3}$$

$$\varepsilon_{z_i z_i}(\theta_i) = \frac{\varepsilon_{yy} + \varepsilon_{zz}}{2} + \sqrt{(\frac{\varepsilon_{yy} - \varepsilon_{zz}}{2})^2 + \gamma_{yz}^2}\,\sin(2\theta_i + \varphi_2)\ (\varphi_2 = \arctan(\frac{\varepsilon_{zz} - \varepsilon_{yy}}{2\gamma_{yz}})) \tag{4}$$

$$\varepsilon_{y_i z_i}(\theta_i) = \sqrt{(\frac{\varepsilon_{yy} - \varepsilon_{zz}}{2})^2 + \gamma_{yz}^2}\,\sin(2\theta_i + \varphi_3)\ (\varphi_3 = \arctan(\frac{2\gamma_{yz}}{\varepsilon_{yy} - \varepsilon_{zz}})) \tag{5}$$

Based on equations 3-4, $\varepsilon_t^{\max} = \bar{\varepsilon} + \gamma_t$ denotes the maximum tract-perpendicular normal strain and $\varepsilon_t^{\min} = \bar{\varepsilon} - \gamma_t$ denotes the minimum tract-perpendicular normal strain, where $\bar{\varepsilon} = (\varepsilon_{yy} + \varepsilon_{zz}) / 2$. Note that in the main text, the $\varepsilon_t^{\max}$ (i.e., the maximum tract-perpendicular normal strain) are reported.

Based on equation 5, we determine the maximum tract-perpendicular shear strain $\gamma_t = \sqrt{\bar{\bar{\varepsilon}}^2 + \gamma_{yz}^2}$, where $\bar{\bar{\varepsilon}} = (\varepsilon_{yy} - \varepsilon_{zz}) / 2$.

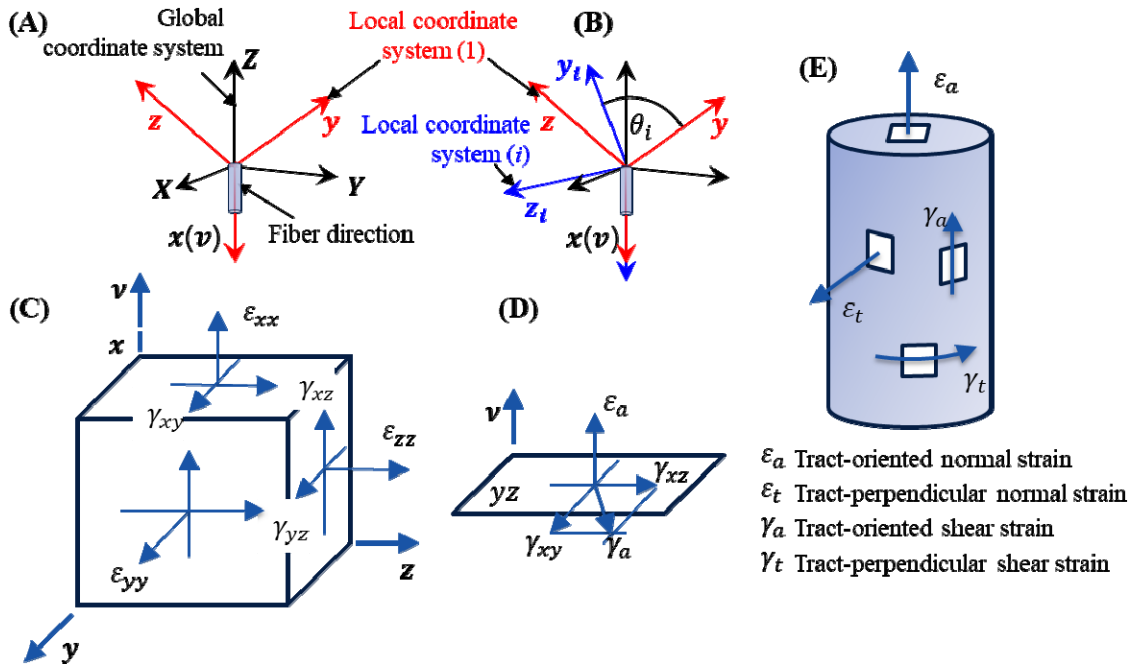

Fig A1. Computation of four tract-related strains via coordinate transformation. (A) Rotate the strain tensor from the global coordinate system (XYZ) to the local coordinate system (1) (xyz), in which x represents the fiber direction (V). (B) Rotate the strain tensor from the local coordinate system (1) to the local coordinate system (*i*) (xy_iz_i). Note that the local coordinate system (*i*) is obtained by rotating the local coordinate system (1) along the fiber direction (V) by arbitrary degree (θ_i). (C) The six independent strain components in the local coordinate system (1). (D) Illustration of ε_{xx}, γ_{xy}, and γ_{xz}, of which the latter two act in the yz plane. (E) Illustration of four tract-related strains that are parameters of interest in the current study, i.e., tract-oriented normal strain ε_a characterizes the normal strain along the fiber tract, tract-perpendicular normal strain ε_t characterizes the maximum normal strain perpendicular to the fiber tract, tract-oriented shear strain γ_a characterizes the shear strain along the fiber tract, and tract-perpendicular shear strain γ_t characterizes the maximum shear strain perpendicular to the fiber tract.

The presented method has been similarly used to compute the orientation-dependent strains in neural cells in *in vitro* models.[64-66,103] We previously used this method to estimate the tract-related deformation during *in silico* impact simulations, in which the real-time fiber orientation (i.e., the deformed fiber orientation that changes at each timestep of the simulation) was used.[51,52] We acknowledge that is flawed and the undeformed fiber orientation should be used (e.g., the static first principal eigenvector of diffusion tensor used in the current study). Errata to our previous studies[51,52] will be published separately.

Appendix B Influence of the disparity of voxel resolution on white matter tract-related strains

To assess how the difference in voxel resolutions (1.5 mm vs. 2.0 mm) affects the tract-related strains, strain tensor data from one randomly selected volunteer test with a spatial resolution of 1.5 mm is down-sampled to 2 mm. Both the original and down-sampled imaging data are used to calculate

the tract-related strains (Fig B1). The similarity in strain contours and overlap in the percentile strain values between two resolutions indicate the spatial resolution disparity (i.e., 1.5 mm vs. 2.0 mm) has negligible effects on four maximum tract-related strains.

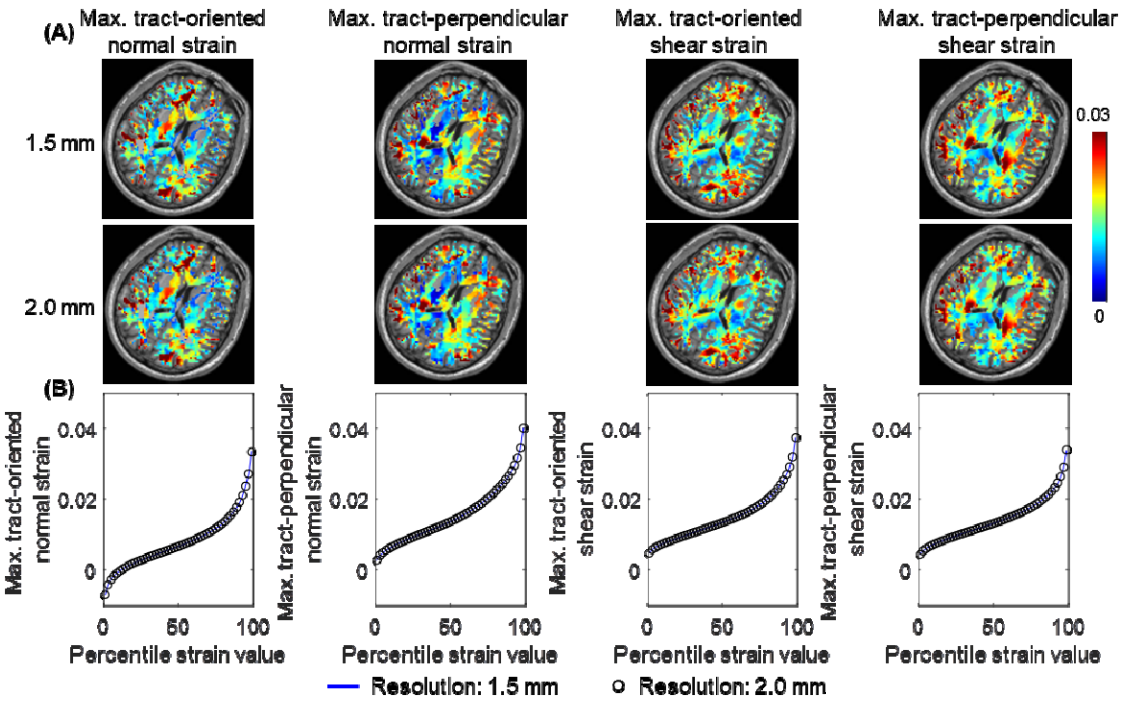

Fig B1. Influence of imaging down-sampling (from 1.5 mm to 2.0 mm) on the maximum values of four tract-related strains in terms of strain distribution (A) and percentile strain values (B).

Appendix C Comparisons of four tract-related strain peaks

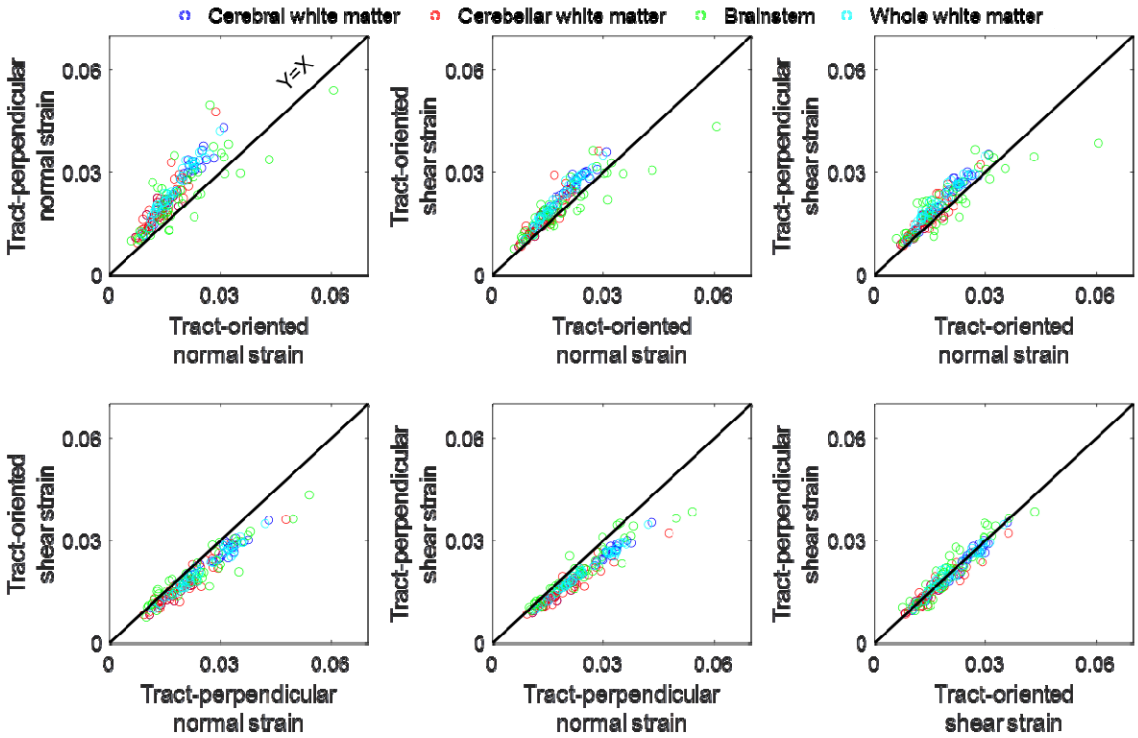

Fig C1. Scatter plots of the peaks of four tract-related strains in the cerebral white matter, cerebellar white matter, brainstem, and whole white matter.